POLITECNICO DI TORINO
Repository ISTITUZIONALE

Accurate evaluation of failure indices of composite layered structures via various FE models

Original
Accurate evaluation of failure indices of composite layered structures via various FE models / de Miguel, A. G.; Kaleel, I.; Nagaraj, M. H.; Pagani, A.; Petrolo, M.; Carrera, E.. - In: COMPOSITES SCIENCE AND TECHNOLOGY. - ISSN 0266-3538. - STAMPA. - 167:(2018), pp. 174-189. [10.1016/j.compscitech.2018.07.031]

Availability:
This version is available at: 11583/2711731 since: 2020-04-24T15:27:00Z

Publisher:
Elsevier

Published
DOI:10.1016/j.compscitech.2018.07.031

Terms of use:

This article is made available under terms and conditions as specified in the corresponding bibliographic description in the repository

Publisher copyright
Elsevier postprint/Author's Accepted Manuscript

© 2018. This manuscript version is made available under the CC-BY-NC-ND 4.0 license http://creativecommons.org/licenses/by-nc-nd/4.0/.The final authenticated version is available online at: http://dx.doi.org/10.1016/j.compscitech.2018.07.031

(Article begins on next page)

12 October 2024

Accurate evaluation of failure indices of composite layered structures via various FE models

A.G. de Miguel[*], I. Kaleel[†], M.H. Nagaraj[‡], A. Pagani[§], M. Petrolo[¶], E. Carrera[‖]

MUL^2 Group, Department of Mechanical and Aerospace Engineering,
Politecnico di Torino, Corso Duca degli Abruzzi 24, 10129 Torino, Italy

Revised version of CSTE_2018_923

Author for correspondence:
E. Carrera, Professor of Aerospace Structures and Aeroelasticity,
MUL^2 Group, Department of Mechanical and Aerospace Engineering,
Politecnico di Torino,
Corso Duca degli Abruzzi 24,
10129 Torino, Italy,
tel: +39 011 090 6836,
fax: +39 011 090 6899,
e-mail: erasmo.carrera@polito.it

[*]Ph.D. Student, e-mail: alberto.garcia@polito.it
[†]Ph.D. Student, e-mail: ibrahim.kaleel@polito.it
[‡]Ph.D. Student, e-mail: manish.nagaraj@polito.it
[§]Assistant Professor, e-mail: alfonso.pagani@polito.it
[¶]Assistant Professor, e-mail: marco.petrolo@polito.it
[‖]Professor of Aerospace Structures and Aeroelasticity, e-mail: erasmo.carrera@polito.it

Abstract

The objective of the current work is to perform a failure evaluation of fiber composite structures based on failure indices computed using the Hashin 3D failure criterion. The analysis employs 1D and 3D finite elements. 1D elements use higher-order structural theories from the Carrera Unified Formulation based on Lagrange expansions of the displacement field. The 3D model analysis exploits ABAQUS. Attention is paid to the free-edge effects, the mode of failure initiation - matrix or fiber tension, delamination -, and the loads at which first ply failure occurs. The results underline the paramount importance of out-of-plane stress components for accurate prediction and the computational efficiency of refined 1D models. In fact, 1D models lead from one to twofold reductions of the CPU time if compared to 3D models.

Keywords: Failure Indices, Hashin 3D, delamination, stress analysis, composites, higher-order models, CUF, free-edge

1 Introduction

Composite materials are increasingly becoming popular for use in engineering structures due to their excellent properties, such as high strength-to-weight and stiffness-to-weight ratios. However, the knowledge regarding failure mechanisms is still incomplete, leading to uncertainties in predicting the probability of failure at a given stress state; this leads to a conservative design via the use of larger safety factors, adding on the weight and reducing the advantages of composite materials.

Failure mechanisms in composite structures are complex phenomena and dependent not only on the constituent material properties, but also geometric features, such as the ply stacking sequence and fiber orientation. The experimental investigation of composite structures for failure analysis is necessary, lengthy and expensive. An attractive alternative is the use of numerical simulations via non-linear finite element analysis (FEA) which, while faster than experimental approaches, still involves significantly high computational costs. For this reason, it can be beneficial to consider linear analyses to estimate the onset of failure [1]. The linear approach makes use of failure criteria to determine the probability of failure point-wise, based on strain and stress states. The magnitude and type of failure predicted by the various failure criteria are generally quantified using failure indices, where a value greater than or equal to unity indicates that failure onset. Early works on the subject involved the use of failure indices to determine the first ply failure load of composite laminates using various polynomial-based failure theories [2, 3]. Other works combined failure indices with genetic algorithms to optimise the stacking sequence [4] and fibre orientation [5] to maximise the load carrying capacity of composite laminates. Failure indices were also used as a design parameter in the failure analysis of adhesively bonded single lap joints in composite laminates [6], failure of pin-loaded composites [7], and the analysis of low velocity impact on thin composite laminates [8]. More recently, failure envelopes have been developed for unidirectional composites using a micromechanical approach based on the High Fidelity Generalised method of Cells (HFGMC) [9].

One of the factors influencing the accuracy of failure indices is the quality of the strain or stress field used in the analysis. For instance, in [2–5], failure indices stemmed from plate models based on the First-Order Shear Deformation Theory (FSDT), whose kinematic assumptions result into a 2D stress state. The use of such 2D stress fields in conjunction with 2D failure theories may not result in accurate values of the failure indices, based on the structure and types of loading considered. A 3D stress analysis may be required to accurately predict the behavior of composite laminates [10]. Such a requirement may severely limit the applicability of reduced dimensional finite element (FE) models such as beams and shells, while a full 3D FEA may be prohibitively expensive due to the sheer number of DOF involved. For this reason, much attention has been paid to the development of refined beam theories to obtain more accurate solutions, without a corresponding increase in the computational size of the problem. For instance, the Generalised Beam Theory makes use of cross-section deformation modes to compute the deformed configuration [11, 12]. On the other hand, the Variational Asymptotic Beam Sectional analysis (VABS) involves the use of asymptotic methods based on a characteristic

parameter to build the series expansion, and hence to refine the beam theory [13]. Other approaches employ warping functions [14], Saint-Venant's solutions [15], and shear correction factors [16].

The current work makes use of refined beam theories based on the Carrera Unified Formulation (CUF) [17]. In this approach, higher-order beam and shell elements are used to develop a high fidelity 1D and 2D model of the structure, resulting into solutions which approach that of 3D FEA in a computationally efficient manner. CUF can accurately predict the 3D stress state of the structural model. Previous works involving CUF were based on the evaluation of failure indices using 2D failure theories where only the in-plane stress components were considered [18], and the evaluation of integral failure indices where a volume instead of a discrete point was considered for the failure index evaluation [19]. The objective of the current work is to perform a failure evaluation of the structure by computing failure indices based on the Hashin 3D failure criteria, using 3D stress fields determined by CUF.

The remainder of the paper is organized in the following manner: Section 2 briefly describes the concept of the CUF. The Hashin 3D Failure Criteria, used to evaluate the failure indices, is summarized in Section 3. Some numerical examples based on standard benchmarks have been presented in Section 4 to demonstrate the capabilities of CUF in predicting failure. Finally, Section 5 presents some conclusions based on the results developed in the current work.

2 The Carrera Unified Formulation

The CUF is a framework to develop higher-order structural theories. In this paper, the 1D CUF was used. The displacement field of a 1D, beam, element in CUF can be denoted as

$$\mathbf{u} = F_\tau(x,z)\mathbf{u}_\tau(y), \tau = 1, 2, \ldots M \tag{1}$$

where $\mathbf{u} = \{u_x, u_y, u_z\}^T$ is the displacement field, $F_\tau(x,z)$ is the expansion function across the cross-section, $\mathbf{u}_\tau$ is the generalized displacement vector, and M is the number of terms in the expansion function. The choice of F_τ and M is arbitrary, i.e., is an input of the analysis. The current work makes use of Lagrange polynomials as F_τ, which is implemented in the form of bi-quadratic 9-node Lagrange cross-sectional elements (L9). The choice of such functions results into theories with purely translational degrees of freedom (DOF), and, thus, the primary unknown variables have a physical meaning, representing translations of structural points in the 3D

space. For instance, in an L9, the displacement field is

$$
\begin{aligned}
u_x &= \sum_{\tau=1}^{9} F_\tau(x,z) u_{x_\tau}(y) \\
u_y &= \sum_{\tau=1}^{9} F_\tau(x,z) u_{y_\tau}(y) \\
u_z &= \sum_{\tau=1}^{9} F_\tau(x,z) u_{z_\tau}(y)
\end{aligned}
\tag{2}
$$

The use of Lagrange elements to discretize the cross-section leads to a 1D FE model in which the physical surfaces can be explicitly modeled without the need for fictitious mathematical entities such as a reference axis [17]. As an example, the 1D CUF model of a 3-ply laminate is shown in Fig. 1, where each ply was modeled with an L9 providing a Layer-Wise description (LW). Furthermore, local refinement of the cross-section, for instance at the interface between two plies, can be easily achieved by the addition of more Lagrange elements [20]. Similarly, more complex configurations can be tackled in which components with varying geometrical and

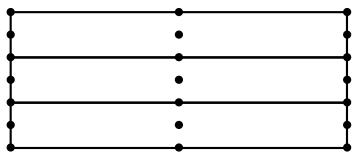

Figure 1: A 3-ply laminate modeled using one L9 element per ply

physical characteristics are modeled via 1D elements leading to a Component-Wise approach (CW) [21].

The stress and strain tensors are defined as

$$
\begin{aligned}
\boldsymbol{\sigma} &= \{\sigma_{xx}, \sigma_{yy}, \sigma_{zz}, \sigma_{xy}, \sigma_{xz}, \sigma_{yz}\}^T \\
\boldsymbol{\varepsilon} &= \{\varepsilon_{xx}, \varepsilon_{yy}, \varepsilon_{zz}, \varepsilon_{xy}, \varepsilon_{xz}, \varepsilon_{yz}\}^T
\end{aligned}
\tag{3}
$$

The linear strain-displacement relation is

$$
\boldsymbol{\varepsilon} = \mathbf{D}\mathbf{u} \tag{4}
$$

where $\mathbf{D}$ is the linear differentiation operator expressed as:

$$
\mathbf{D} = \begin{bmatrix}
\frac{\partial}{\partial x} & 0 & 0 \\
0 & \frac{\partial}{\partial y} & 0 \\
0 & 0 & \frac{\partial}{\partial z} \\
\frac{\partial}{\partial y} & \frac{\partial}{\partial x} & 0 \\
\frac{\partial}{\partial z} & 0 & \frac{\partial}{\partial x} \\
0 & \frac{\partial}{\partial z} & \frac{\partial}{\partial y}
\end{bmatrix}
$$

The stress-strain relations are described by the elastic constitutive law, and are given by

$$\boldsymbol{\sigma} = \mathbf{C}\boldsymbol{\varepsilon} \tag{5}$$

where $\mathbf{C}$ is the linear elastic material coefficient matrix defined in the global system [22].

The structure is discretized along the axial direction with standard beam elements, interpolated using the nodal shape functions N_i. In this paper, three and four node beam elements were used and referred to as B3 and B4, respectively. The use of beam elements along the axis, along with L9 across the cross-section, results in the following 3D displacement field:

$$\mathbf{u}(x, y, z) = F_\tau(x, z)N_i(y)\mathbf{u}_{\tau i} \tag{6}$$

where $\mathbf{u}_{\tau i}$ is the nodal displacement field. According to the principle of virtual displacements,

$$\delta L_{int} = \delta L_{ext} \tag{7}$$

where δL_{int} is the virtual variation of the internal strain energy,

$$\delta L_{int} = \int_V \delta\boldsymbol{\varepsilon}^T\boldsymbol{\sigma} \tag{8}$$

L_{ext} is the work due to external loading,

$$L_{ext} = F_s N_j \delta\mathbf{u}_{sj}^T\mathbf{P} \tag{9}$$

where $\mathbf{P}$ is the external force vector. The virtual variation of the internal strain energy can be formulated using Eqs. (5), (6) and (8), which results in the following equation for the stiffness matrix:

$$\delta L_{int} = \delta\mathbf{u}_{sj}^T\mathbf{k}_{ij\tau s}\mathbf{u}_{\tau i} \tag{10}$$

with

$$\mathbf{k}_{ij\tau s} = \int_l\int_\Omega \mathbf{D}^T(N_i(y)F_\tau(x, z))\mathbf{C}\mathbf{D}(N_j(y)F_s(x, z))\ d\Omega\ dl \tag{11}$$

where Ω denotes the cross-sectional domain, and l is the length of the structure in the axial direction. $\mathbf{k}_{ij\tau s}$ is the 3x3 Fundamental Nucleus (FN) and remains invariant with respect to the order of beam element and choice of expansion function across the section. Assembling the FNs calculated by looping through the indices $\{i, j, \tau, s\}$ results in the element stiffness matrix. A more detailed explanation of the concept of the fundamental nucleus and its role in CUF can be found in [17].

3 Evaluation of failure indices

Failure indices are evaluated using the Hashin 3D failure criteria for the prediction of ply failure, and the mixed mode quadratic criteria to determine the onset of delamination. The failure indices are defined using the stress state in the material coordinate system, as shown in Fig. 2.

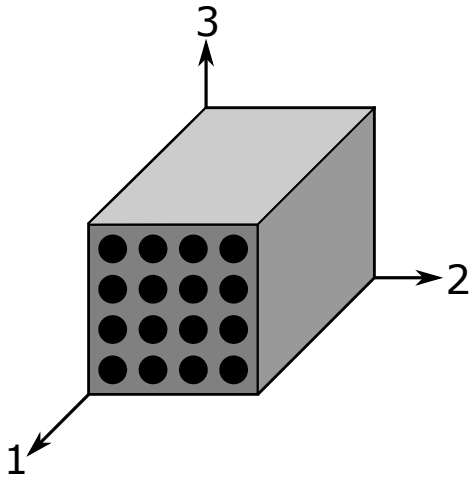

Figure 2: The material coordinate system oriented in the direction of the fibre

The Hashin 3D failure criteria [23] are used to determine first ply failure based on the stress state and to determine the dominating failure mode at the ply level. The failure indices for the state of matrix and fiber tension or compression are computed according to the following equations:

1. Fibre Tension:

$$\left(\frac{\sigma_{11}^2}{X_T}\right)^2 + \frac{\sigma_{12}^2 + \sigma_{13}^2}{S_{12}^2} \geq 1 \tag{12}$$

2. Fibre Compression:

$$\left(\frac{\sigma_{11}^2}{X_C}\right)^2 \geq 1 \tag{13}$$

3. Matrix Tension:

$$\frac{(\sigma_{22} + \sigma_{33})^2}{Y_T^2} + \frac{\sigma_{23}^2 - \sigma_{22}\sigma_{33}}{S_{23}^2} + \frac{\sigma_{12}^2 + \sigma_{13}^2}{S_{12}^2} \geq 1 \tag{14}$$

4. Matrix Compression:

$$\left[\left(\frac{Y_C}{2S_{23}}\right)^2 - 1\right]\left(\frac{\sigma_{22} + \sigma_{33}}{Y_C}\right) + \frac{(\sigma_{22} + \sigma_{33})^2}{4S_{23}^2} + \frac{\sigma_{23}^2 - \sigma_{22}\sigma_{33}}{S_{23}^2} + \frac{\sigma_{12}^2 + \sigma_{13}^2}{S_{12}^2} \geq 1 \tag{15}$$

where σ_{ij} represents the components of the stress tensor in the material coordinate system. X represents the material strength in the fiber direction, and Y represents that of the transverse direction, with the subscripts T and C denoting tensile and compressive loading, respectively. S_{ij} denotes the material shear strengths.

The delamination index is determined based on the mixed mode quadratic criterion [24], and is given by:

$$\left(\frac{<\sigma_{33}>}{Z_T}\right)^2 + \left(\frac{\sigma_{23}}{S_{23}}\right)^2 + \left(\frac{\sigma_{13}}{S_{13}}\right)^2 \geq 1 \tag{16}$$

where $<\sigma 33>$ denotes $max(0, \sigma_{33})$, σ_{33} being the transverse normal stress in the material coordinate system. σ_{13} and σ_{23} are the transverse shear stresses, Z_T is the interlaminar normal strength while S_{13} and S_{23} are the transverse shear strengths.

4 Numerical Examples

4.1 Tensile tests

A failure index evaluation of a tensile specimen was carried out as an initial assessment of the proposed formulation. First, a balanced and symmetric cross-ply was considered based on the recommendations of ASTM 3039 [25] and the solutions obtained from CUF were compared with those of 3D FEA generated in the commercial software ABAQUS. Then, the delamination onset was studied on $[\theta/-\theta]_s$ specimens and compared with semi-analytical and experimental results available in the literature. Two material systems were considered: IM7/8552 and G947/M18 fiber composites, whose material properties are listed in Table 1.

Material	E_1 [GPa]	E_2 [GPa]	E_3 [GPa]	G_{12} [GPa]	G_{13} [GPa]	G_{23} [GPa]	ν_{12}	ν_{13}	ν_{23}
IM7/8552	165.0	9.0	9.0	5.6	5.6	2.8	0.34	0.34	0.5
G947/M18	97.6	8.0	8.0	3.1	3.1	2.7	0.37	0.37	0.5

Table 1: Mechanical properties of the IM7/8552 and G947/M18 material systems

4.1.1 3D assessment of a $[45/\text{-}45/90/0]_s$ specimen

For the first numerical assessment, a uni-axial tension test on a symmetric cross-ply specimen was considered. The material selected was IM7/8552, with a stacking sequence of $[45, \text{-}45, 90, 0]_s$. The recommended dimensions [25] were employed; $L = 200$ mm, $b = 25$ mm and $h = 2.54$ mm, with the thickness of each lamina being equal to $h_0 = 0.3175$ mm. A schematic representation of the specimen and the boundary conditions are given in Fig. 3. On one end [y = 0.0], the displacements in the y and z directions were constrained, while in the other [y = L] simply-supported conditions were applied on the z direction. Symmetry on the x axis is imposed. A longitudinal force of magnitude $F = 6,350$ N was applied at y = L.

The accuracy of the various models in computing the full set of stress components, and subsequently the failure indices, was evaluated. The three predominant failure modes which can arise in a tensile test were addressed: delamination onset, matrix failure, and fiber failure. The former mode was calculated making use of the mixed mode quadratic criteria, whereas the latter two were based on the Hashin 3D criteria.

The main aim of the present study is to demonstrate the efficiency and fidelity of the stress solutions

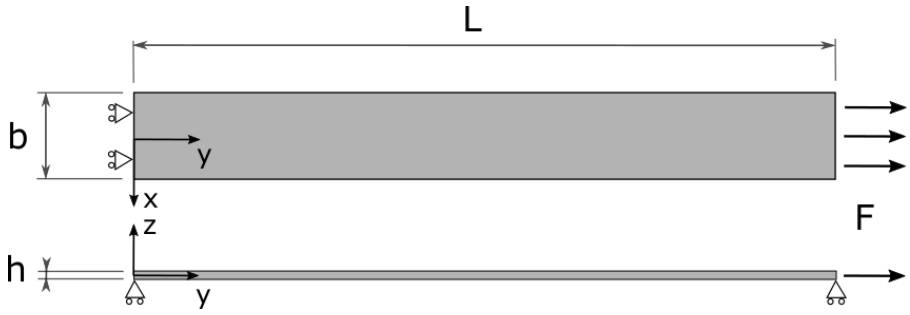

Figure 3: Dimensions and loading conditions of the tensile specimen

obtained with the CUF-LW models in comparison with solid models. The stress solutions of the proposed model were evaluated at relevant points through the thickness within the structure, along with a mesh convergence study; center of the beam [x = 0.0, y = L/2], and free-edge at the mid-span [x = 12.5, y = L/2]). In the analysis, attention was paid to the out-of-plane stress components, which directly influence the onset of failure in composite materials. The model data and computational times for both CUF and ABAQUS models are tabulated in Table 2. The main differences between the modeling procedure followed in a CUF-LW model and a 3D model are illustrated in Fig. 4. In the former, the discretization of the cross-section domain remains independent of the longitudinal mesh, therefore, allowing refinements of the cross-section with a reduced impact in the total size of the computational problem. This is in strong contrast with standard 3D solid models, where the necessity of maintaining a suitable aspect ratio of the FE along all 3 directions may result in a very fine discretisation along the model axis, thus increasing computational costs.

Table 2: Model information for the tensile specimen

Model	Discretization*	DOF	CPU Time [s]
CUF-LW	320 L9 over the cross-section, with 6 B4 along y.	77,805	82
ABQ3D-Coarse	Linear brick elements (C3D8) with a mesh of 30 x 8 x 200 elements. One element per layer.	168,237	27
ABQ3D-Medium	Linear brick elements (C3D8) with a mesh of 30 x 24 x 200 elements. Three elements per layer.	467,325	261
ABQ3D-Refined	Linear brick elements (C3D8) with a mesh of 70 x 40 x 400 elements. Five elements per layer.	3,501,933	3526

*All discretizations are graded towards the free-edges

Figure 5 shows the in-plane stresses through the thickness at [x = 0.0, y = L/2], i.e., at the center of the midspan, while Fig. 6 shows the out-of-plane stresses through the thickness at [x = 12.5, y = L/2], i.e., at the free-edge of the midspan.

The following procedure was chosen to compare the accuracy of the various numerical models for the failure evaluation: first, the CUF-LW model was run and, for each failure mode - delamination, matrix tension and fiber tension - the axial load of failure onset was computed. Subsequently, the computed loads were applied to the 3D models, and the failure indices obtained were presented for comparison. The material strengths are shown in Table 3. The results are shown in Table 4. Subsequently, the tensile loads at which the different failure

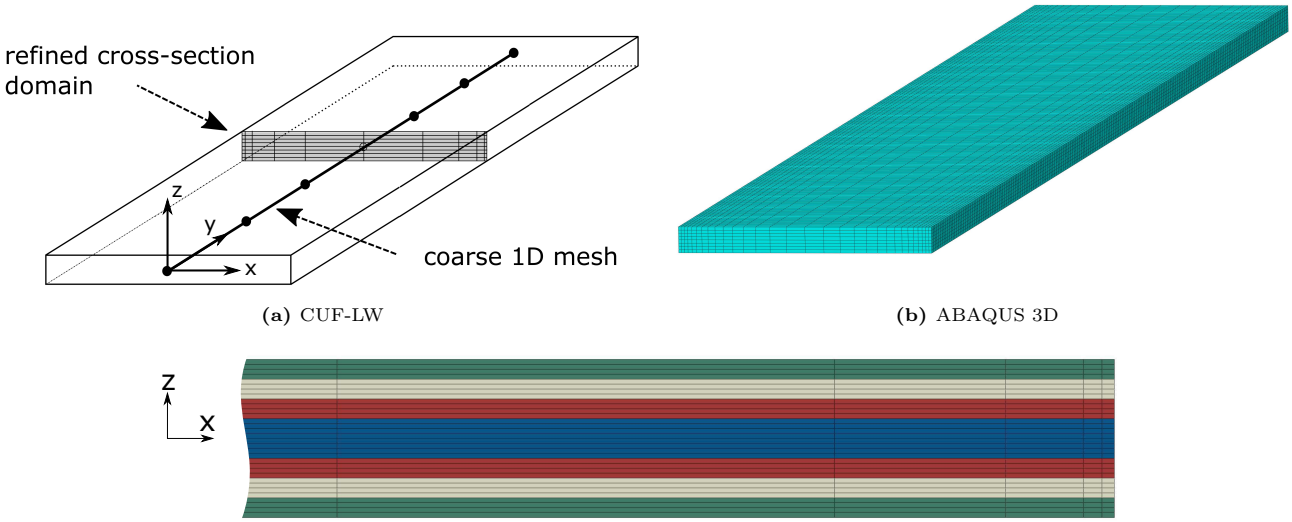

(a) CUF-LW

(b) ABAQUS 3D

(c) CUF cross-section mesh

Figure 4: Comparison between the beam and solid discretization. The CUF cross-section mesh is schematically represented in (c), where due to symmetry, only the right half is shown.

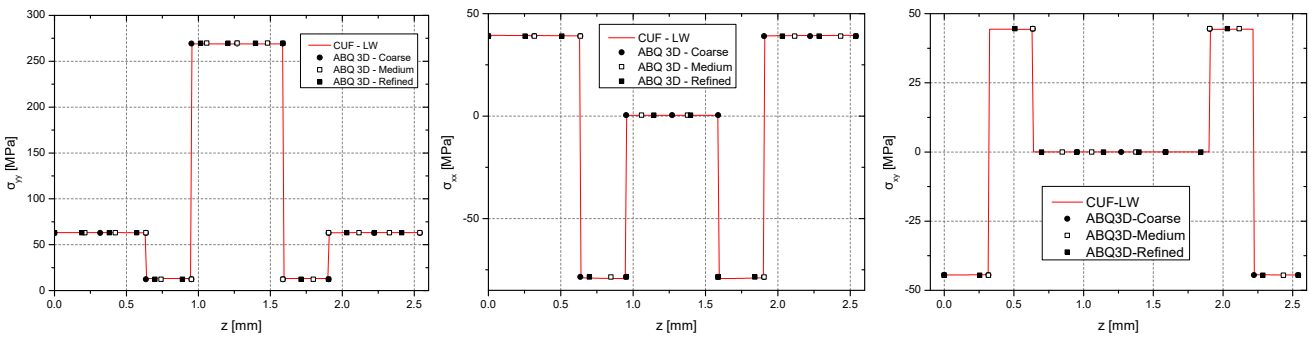

(a) σ_{yy}

(b) σ_{xx}

(c) σ_{xy}

Figure 5: In-plane stress components at the centre of the section.

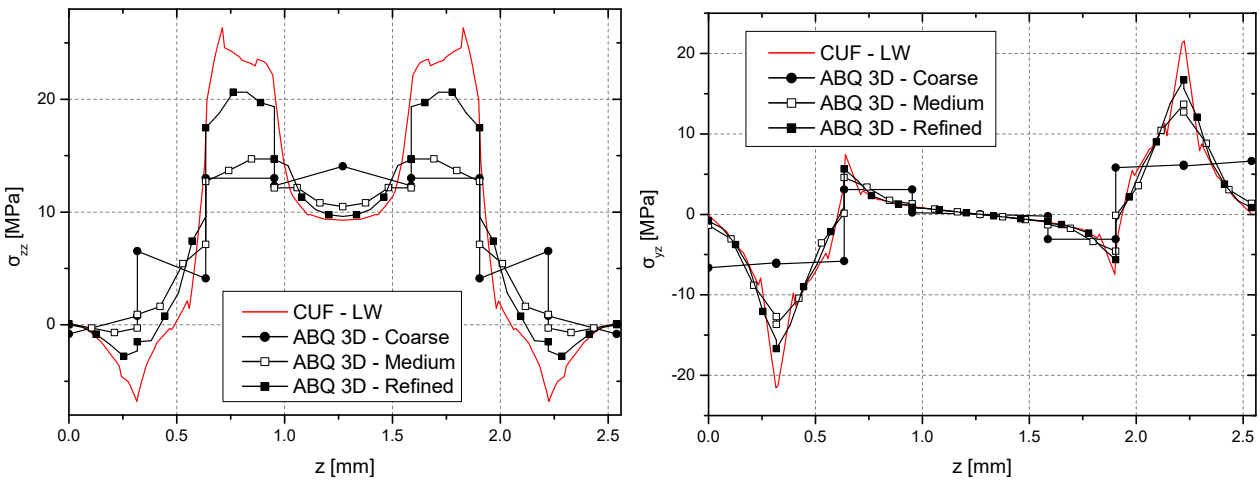

(a) σ_{zz}

(b) σ_{yz}

Figure 6: Out-of-plane stress components at the free-edge

indexes reach the unit value are shown in Table 5. It is worth mentioning that the present study is based on linear analyses. Therefore, the failure modes remain independent of each other, i.e., the onset of a given mode does not influence the others.

Table 3: Material strength values of the IM7/8552 composite

Failure criteria	Z_t [MPa]	S_{13} [MPa]	S_{23} [MPa]	X_t [MPa]	Y_t [MPa]	S_{12} [MPa]
Mixed mode delamination	60.0	90.0	90.0			
Hashin 3D	73.0	90.0	57.0	2,560.0	73.0	90.0

Table 4: Comparison of the failure indices computed by the different models considered under the same loading value

Mode		Delamination	Matrix Tension	Fibre Tension	Fiber Tension*
Load [N]		14,287.5	11,938.0	27,178.0	34,417.0
Model	DOF	Failure index value			
ABQ3D coarse	168,237	0.28	0.4	0.7	1.07
ABQ3D medium	467,325	0.31	0.45	0.71	0.94
ABQ3D refined	3,501,933	0.6	0.73	0.82	1.05
CUF-LW	77,805	1	1	1	1

*Modified Hashin 3D criteria with only in-plane components

Table 5: Values of the tensile load corresponding to the onset of failure of each mode considered

Mode	DOF	Delamination	Matrix Tension	Fibre Tension	Fiber Tension*
ABQ3D coarse	168,237	27,178.0	18,796.0	32,385.0	33,401.0
ABQ3D medium	467,325	25,717.5	17,843.5	32,258.0	35,433.0
ABQ3D refined	3,501,933	18,478.5	14,033.5	30,226.0	33,655.0
CUF-LW	77,805	14,287.5	11,938.0	27,178.0	34,417.0

*Modified Hashin 3D criteria with only in-plane components

Figures 7-9 show the 3D plots of the failure indices for the CUF-LW and the finest solid model. In the case of the fiber failure based on the Hashin 3D criteria, Fig. 9, the free-edge effects cause the fibers to fail at the interfaces in the free-edge due to the high interlaminar stresses, see Fig. 6. To avoid this non-physical response and evaluate the effect of shear, a modified Hashin criterion was proposed which neglects the transverse shear stresses, σ_{yz}. The corresponding results of fiber failure are included in Table 4, as well as in Fig. 10.

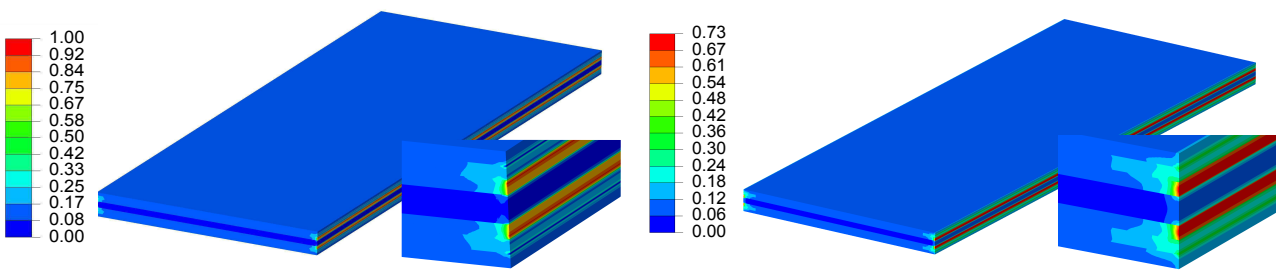

(a) CUF-LW **(b)** ABQ3D - refined

Figure 7: Failure index for matrix tension

The following observations can be made based on the obtained results:

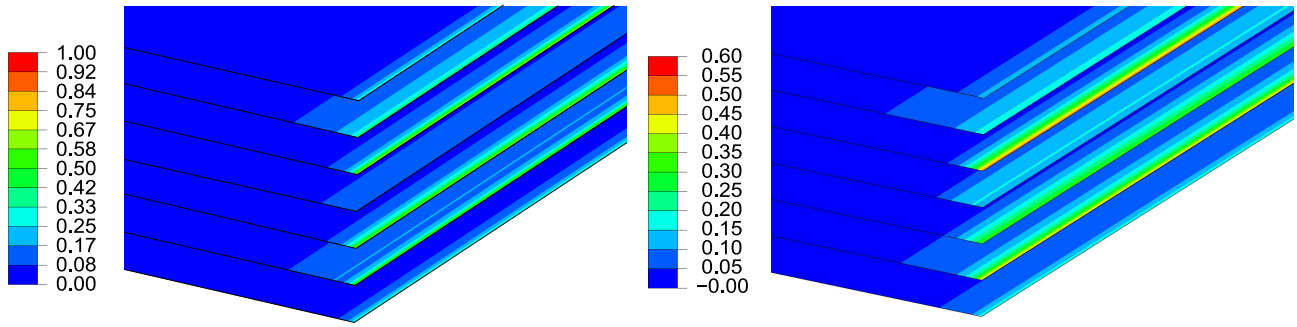

(a) CUF-LW **(b)** ABQ3D - refined

Figure 8: Failure index for delamination

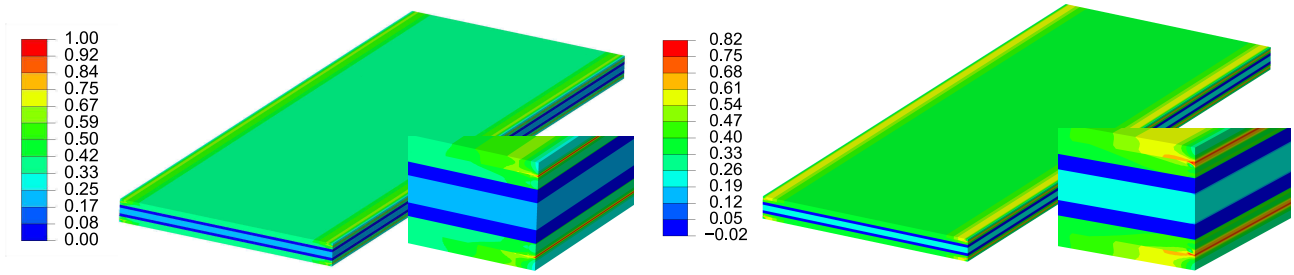

(a) CUF-LW **(b)** ABQ3D - refined

Figure 9: Failure index for fiber tension

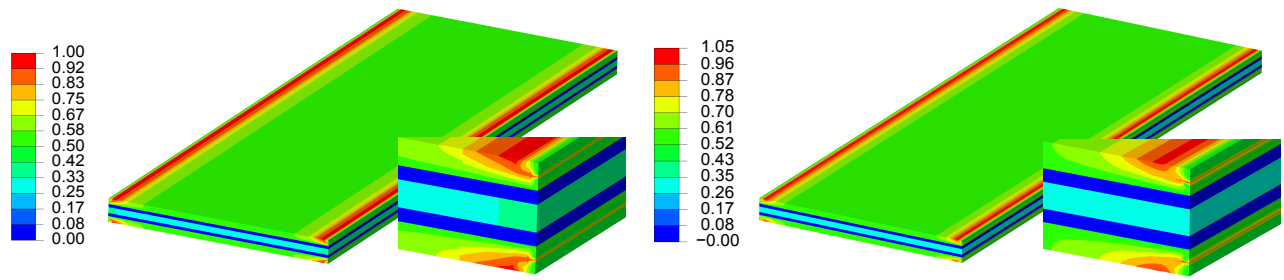

(a) CUF-LW **(b)** ABQ3D - refined

Figure 10: Failure index for fiber tension using the modified criterion

1. All models provide the same solutions for in-plane stresses but differences arise in the evaluation of the out-of-plane stress components at the free-edge.

2. The correct computation of the 3D failure indices is strongly related to the accuracy of the out-of-plane stresses. If the 3D stress fields are not computed to a sufficient level of accuracy in the critical zones of the structure, e.g., free-edges, the values of the failure indices may vary to a great extent. This effect is more noticeable for the matrix and interface failures, see Tables 4 and 5.

3. In the 3D models, the mesh refinement has a strong influence on the failure index evaluation. In particular, refined meshes are necessary for the out-of-plane components of stresses.

4. The refinement of the CUF models is required at the cross-section level only. i.e., the refinement of the structural theory, instead of the 3D mesh, leads to very accurate 3D stress fields and some twenty times as less DOF as for the 3D model.

5. The detection of σ_{zz} peak values at the free-edges is particularly challenging and, usually, such peaks are due to the presence of inner 90-layers as mentioned in [26, 27].

4.1.2 $[\theta,-\theta]_s$ specimens under tensile load

The second assessment deals with the delamination onset of $[\theta_n,-\theta_n]_s$ specimens made of G947/M18 under an axial extension, ε_0. The assessment aims to verify and validate the present formulation against other numerical results and experimental texts, respectively. Since only $[\theta_n,-\theta_n]_s$ cases were considered and no further analyses were carried out, the results of this section are considered are complementary of those of Section 4.1.1.

The problem features were taken from the work of Lagunegrand et al. [28], who performed experimental tests on this class of specimens to evaluate the delamination initiation via acoustic measurements and semi-analytical models. The geometry and loading conditions are equivalent to those of Fig. 3 with the following dimensions: $L = 400$ mm and $b = 20$ mm. The thickness of the G947/M18 ply is equal to $h_0 = 0.19$ mm, and the effect of the total thickness of the laminate, h, on the onset of delamination was studied.

Figure 11 shows the interlaminar shear stress in the vicinity of the free-edge [y = L/2, z = h_0] for the $[+10,-10]_s$ specimen. Two section refinements were considered: 10 × 20 L9 with a total of 49,077 DOF (CUF-LW_1) and 14 × 24 L9 with 80,997 DOF (CUF-LW_2). The results of the CUF analysis were compared with semi-analytical solutions of the software CLEOPS from Lagunegrand et al. [28], which is based on the boundary layer method, and a 2D plane strain model and 3D model from the work of Martin et al. [29]. The 2D model of the latter reference was generated using linear triangular elements (20,000 nodes) and a minimum element length of 1 μm in the free edge, whereas the 3D model was generated using tetrahedral elements and a minimum element size of 10 μm. In Fig. 12, it can be observed the concentration of transverse stresses in the interfaces between the [+10] and [-10] plies. Based on the premises of [28], delamination by pure mode III was considered in this example, i.e., the effects of σ_{zz} were considered negligible in the failure criteria. Accordingly, the curves of the

applied load causing the delamination initiation for the laminates $[+10_n,\text{-}10_n]_s$, $[+20_n,\text{-}20_n]_s$ and $[+30_n,\text{-}30_n]_s$ with an increasing thickness ($n = 1, 2, 3, 4$) are shown in Fig. 13 and compared against the experimental results.

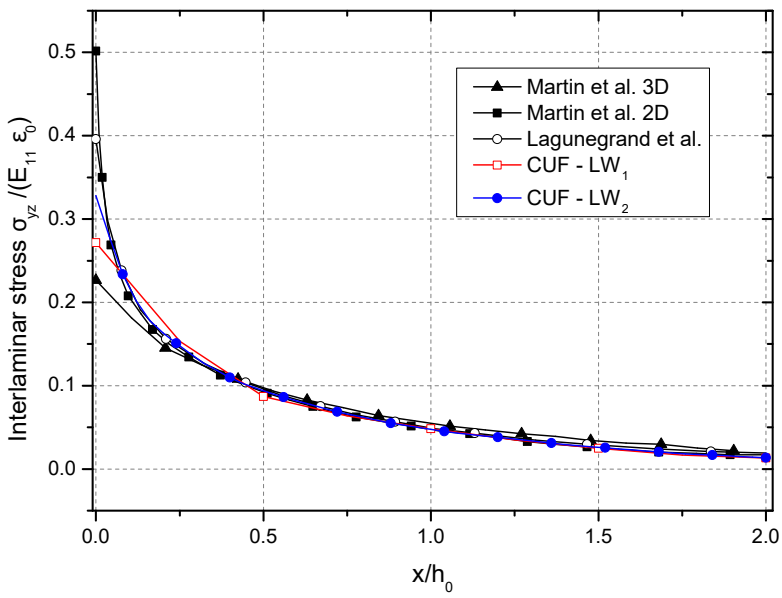

Figure 11: Normalized interlaminar shear stress of the G947/M18 $[+10,\text{-}10]_s$ specimen under axial extension

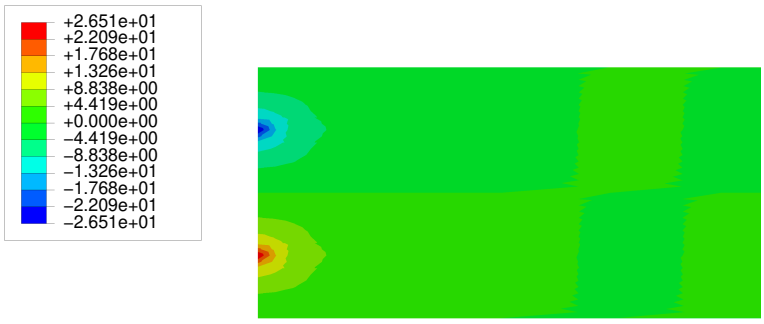

Figure 12: Plot of the transverse shear stresses [MPa] in the vicinity of the free-edge of the G947/M18 $[+10,\text{-}10]_s$ specimen for a uniform extension of $\varepsilon_0 = 0.001$

The results suggest that:

1. The present formulation can provide accurate free-edge transverse shear stresses. In fact, results match very well with those from other models in literature and experiments.

2. Localized failure can be captured, and the delamination onset was determined accurately.

3. As well-known, the free-edge effects are very localized and tend to disappear as soon as a distance roughly equal to the total thickness of the laminate is considered.

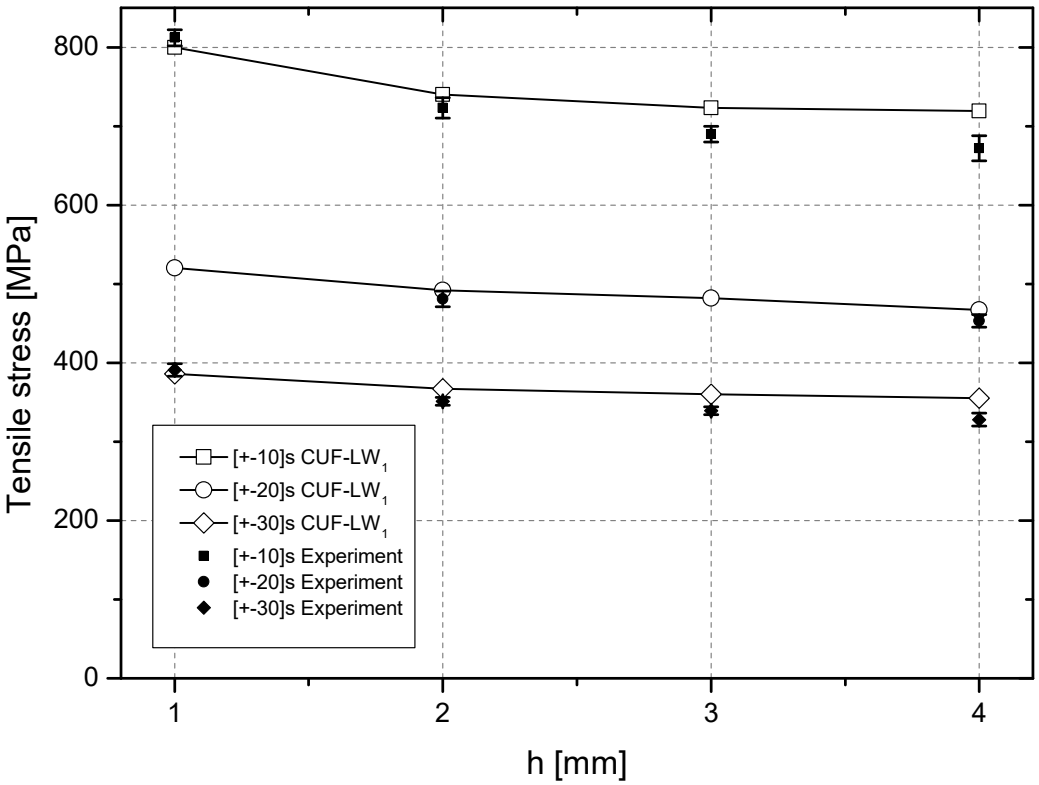

Figure 13: Comparison of the delamination onset in the G947/M18 specimen obtained from the proposed model and the experiments [28]

4.2 Plate with a hole

In the current example, a rectangular plate with a central hole was considered. The plate dimensions are the following: L = 138.0 mm, w = 38.1 mm, and hole diameter d = 6.34 mm. The plate is clamped on one end, and displacement is prescribed on the opposite end. The geometry and boundary conditions of the notched specimen are shown in Fig. 14. Three lamination sequences were considered, namely [0], [90] and $[0/90]_s$. As illustrated in Fig. 15, CUF-LW notched specimens were modeled as a three-component beam assembly. The components can be easily connected to the interfaces because of the use of CUF-LW results in only displacement DOF. In particular, at the interface, the continuity of displacement field is enforced via the shared nodes, as shown in Fig. 15. Further details on the approach to combine 1-, 2- and 3-dimensional refined models in the CUF framework can be found in [21]. The far-notch beam configuration was modeled with a combination of B4 beam elements along with L9 cross-section elements, where the beam is oriented in the y-direction. Each far-notch zone spans 49 mm in length. A combination of B3 beam elements along with L9 elements was employed to model the near-notch region. Various 3D FEM models with varying degrees of mesh refinement were built in ABAQUS for comparison purposes. Table 6 lists the mesh data for various models in CUF and ABAQUS.

The load required for the first ply failure was determined for the models described in Table 6, where the load corresponds to the value at which one of the failure indices attains the value of unity. In all the analyses, displacement boundary conditions were prescribed, and the corresponding load is computed in order to obtain the load at first ply failure. Table 7 tabulates the first ply failure load along with the mode of failure, for various

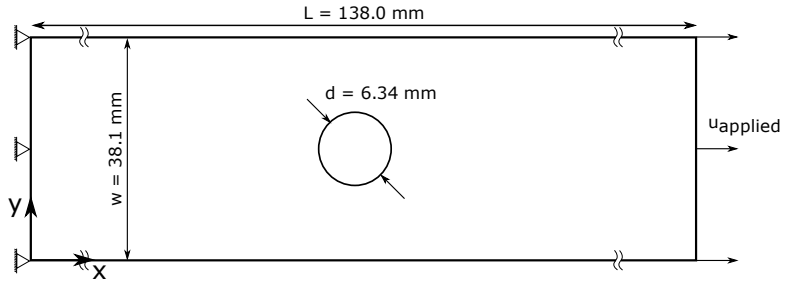

Figure 14: Geometry and boundary conditions for failure evaluation of notched composite specimens

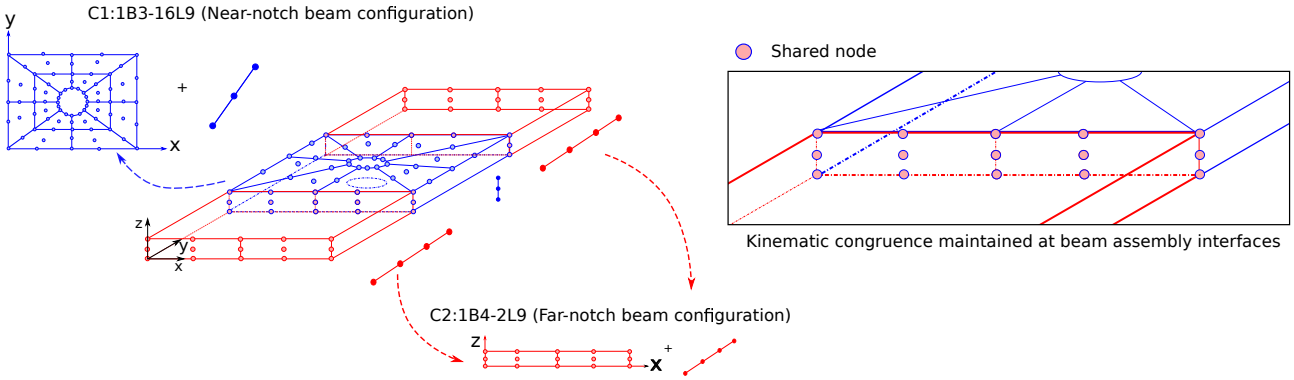

Figure 15: Modeling of notched composite specimens using refined 1D CUF-LW models

Table 6: Model information for failure index evaluation of notched composite specimens

Model	Discretization	DOF	CPU Time (s)
Laminate 1 : [0]			
CUF-LW	C2: 7L9-10B4 and C1:136L9-1B3 (One element per layer)	9,414	4
ABQ3D-Coarse	Linear brick elements (C3D8) with an average element size of 0.275 around the notch. Two elements per layer.	25,632	6
ABQ3D-Refined	Linear brick elements (C3D8) with an average element size of 0.2 around the notch. Two elements per layer.	39,348	12
Laminate 2 : [90]			
CUF-LW	C2: 7L9-10B4 and C1:136L9-1B3 (One element per layer)	9,414	4
ABQ3D-Coarse	Linear brick elements (C3D8) with an average element size of 0.275 around the notch. Two elements per layer.	25,632	6
ABQ3D-Medium	Linear brick elements (C3D8) with an average element size of 0.2 around the notch. Two elements per layer.	39,348	7
ABQ3D-Refined	Linear brick elements (C3D8) with an average element size of 0.1 around the notch. Two elements per layer.	93,960	15
Laminate 3 : $[0/90]_s$			
CUF-LW1	C2: 28L9-10B4 and C1:136L9-4B3 (One element per layer)	28,242	19
CUF-LW2	C2: 56L9-10B4 and C1:136L9-8B3 (Two elements per layer)	53,346	42
ABQ3D-1L	Linear brick elements (C3D8) with an average element size of 0.1 around the notch. One element per layer.	187,320	42
ABQ3D-2LQ	Quadratic brick elements (C3D20) with an average element size of 0.2 around the notch. Two element per layer.	265,782	68
ABQ3D-4LR	Linear brick elements (C3D8) with an average element size of 0.05 around the notch. Four elements per layer.	1,306,977	602

models of notched composite specimens. The normal in-plane stress distributions at the top of the layer and along the width of the notched composite laminate for the [0] and [90] specimens were plotted in Fig. 16a and Fig. 16b, respectively. The contour plot of the Hashin-3D matrix tension failure index for the [0] laminate has been given in Fig. 17, for an applied displacement of 0.2 mm which corresponds to first ply failure. Similarly, first ply failure occurs for a displacement of 0.45 mm in the case of the [90] laminate, and the contour plot of the Hashin-3D matrix tension failure index has been given in Fig. 18. The axial stress σ_{yy} through the thickness of the $[0/90]_s$ notched laminate was plotted in Fig. 19. Similarly, the transverse shear stresses σ_{xy} and σ_{yz} were plotted in Fig. 20 and Fig. 21, respectively. The contour plots of the Hashin-3D matrix tension and the delamination failure indices, for the $[0/90]_s$ laminate under an applied displacement of 0.125 mm, were plotted in Fig. 22 and Fig. 23, respectively.

Table 7: Numerical results for load at first ply failure for different models of notched composite specimens

Model	DOF	Load at first ply failure [N]	First ply failure mode
Laminate 1 : [0]			
CUF-LW	9,414	1,120	
ABQ3D-Coarse	25,632	1,142	Matrix Tension
ABQ3D-Refined	39,348	1,120	
Laminate 2 : [90]			
CUF-LW	9,414	141	
ABQ3D-Coarse	25,632	147	Matrix Tension
ABQ3D-Medium	39,348	146	
ABQ3D-Refined	93,960	141	
Laminate 3 : $[0/90]_s$			
CUF-LW1	28,242	1,531	
CUF-LW2	53,346	1,500	
ABQ3D-1L	187,320	2,097	Matrix Tension
ABQ3D-2LQ	265,782	1,737	
ABQ3D-4LR	1,306,977	1,797	

Based on the above results, the following observations can be made regarding the analysis of notched composites:

1. The CUF results for the in-plane stress components agree well with those of the ABAQUS 3D solutions, as can be seen in Fig. 16a and Fig. 16b for the [0] and [90] ply laminates, respectively.

2. It can be seen in Fig. 17 and Fig. 18 that the failure indices obtained from the CUF analysis are slightly higher than that obtained from ABAQUS. This is significant since it infers that initial failure occurs earlier i.e. at a lower magnitude of the applied load, than is predicted by ABAQUS.

3. In the case of the $[0/90]_s$ laminate, it can be seen from Fig. 20 and Fig. 21 that the in-plane shear stresses

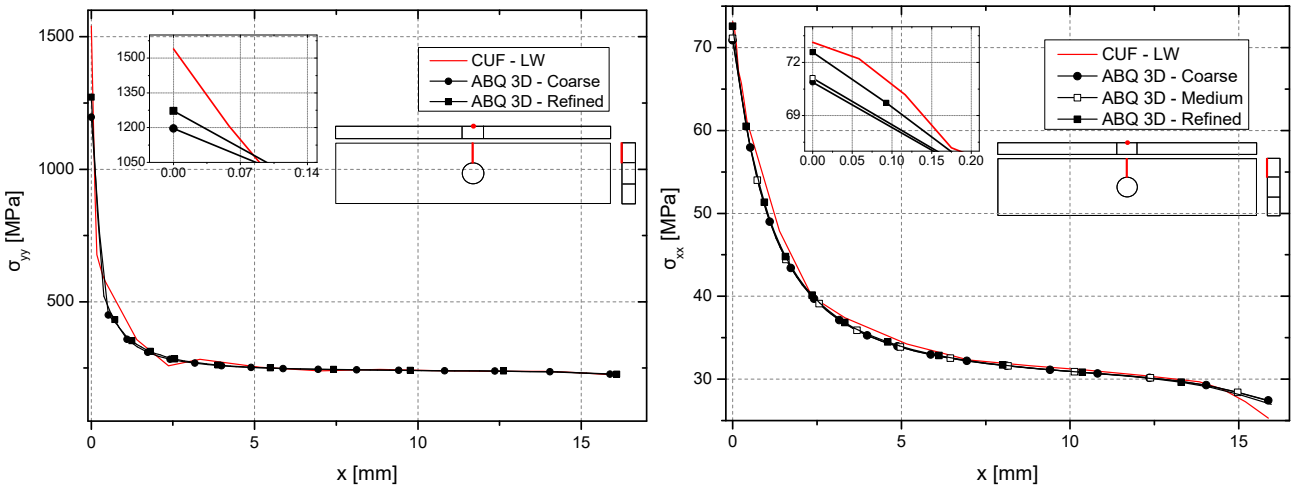

(a) σ_{yy} for [0] laminate under an applied displacement of 0.2 mm **(b)** σ_{xx} for [90] laminate under an applied displacement of 0.4 mm

Figure 16: Normal stress distribution along the width of notched composite specimen,

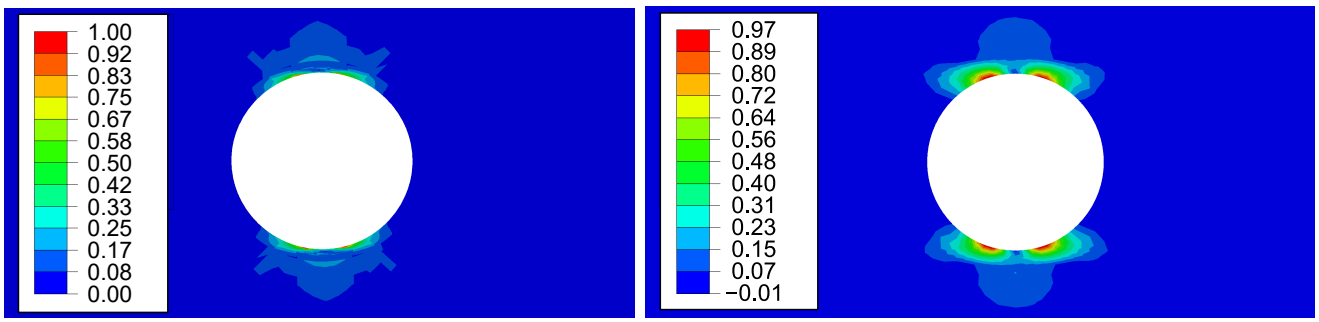

(a) CUF-LW (9,414 DOF) **(b)** ABQ3D-Refined (39,348 DOF)

Figure 17: Hashin3D matrix tension (MT) failure index for [0] laminate under an applied displacement of 0.2 mm

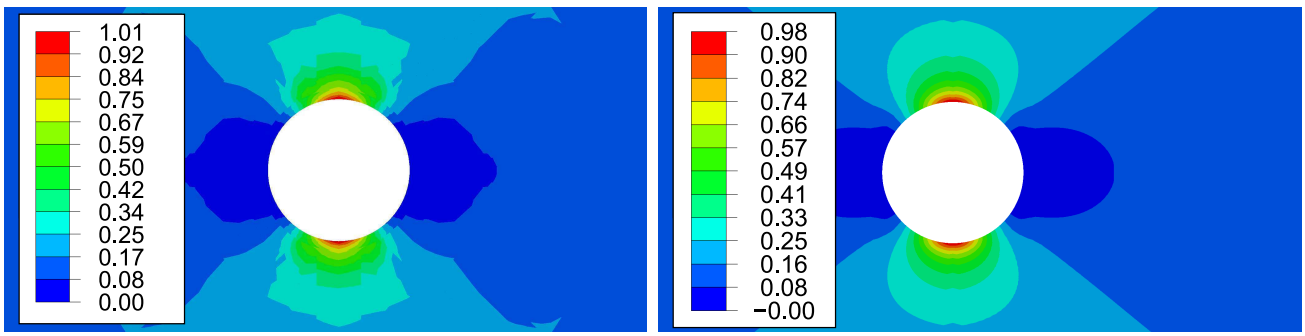

(a) CUF-LW (9,414 DOF) **(b)** ABQ3D-Refined (93,960 DOF)

Figure 18: Hashin3D matrix tension (MT) failure index for [90] laminate under an applied displacement of 0.45 mm

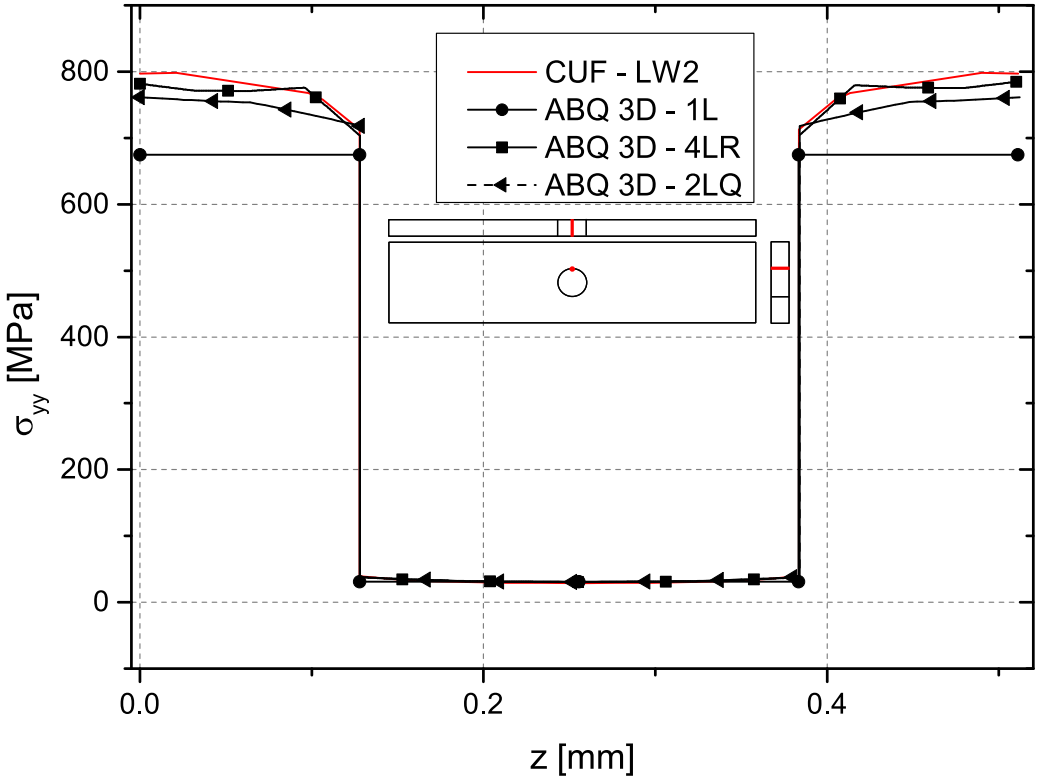

Figure 19: Normal stress distribution σ_{yy} through the thickness of $[0/90]_s$ notched laminate under an applied displacement of 0.125 mm, $x = 16.875$, $y = 69$

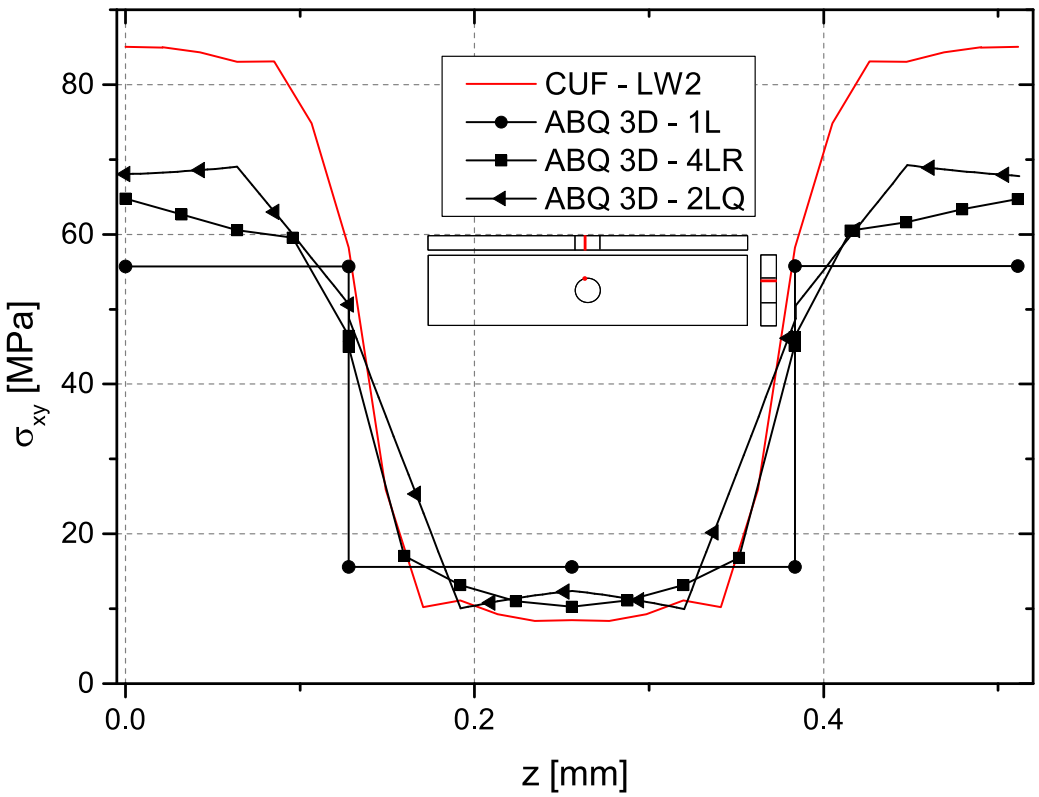

Figure 20: In-plane shear stress distribution σ_{xy} through the thickness of $[0/90]_s$ notched laminate under an applied displacement of 0.125 mm, $x = 16.875$, $y = 69$

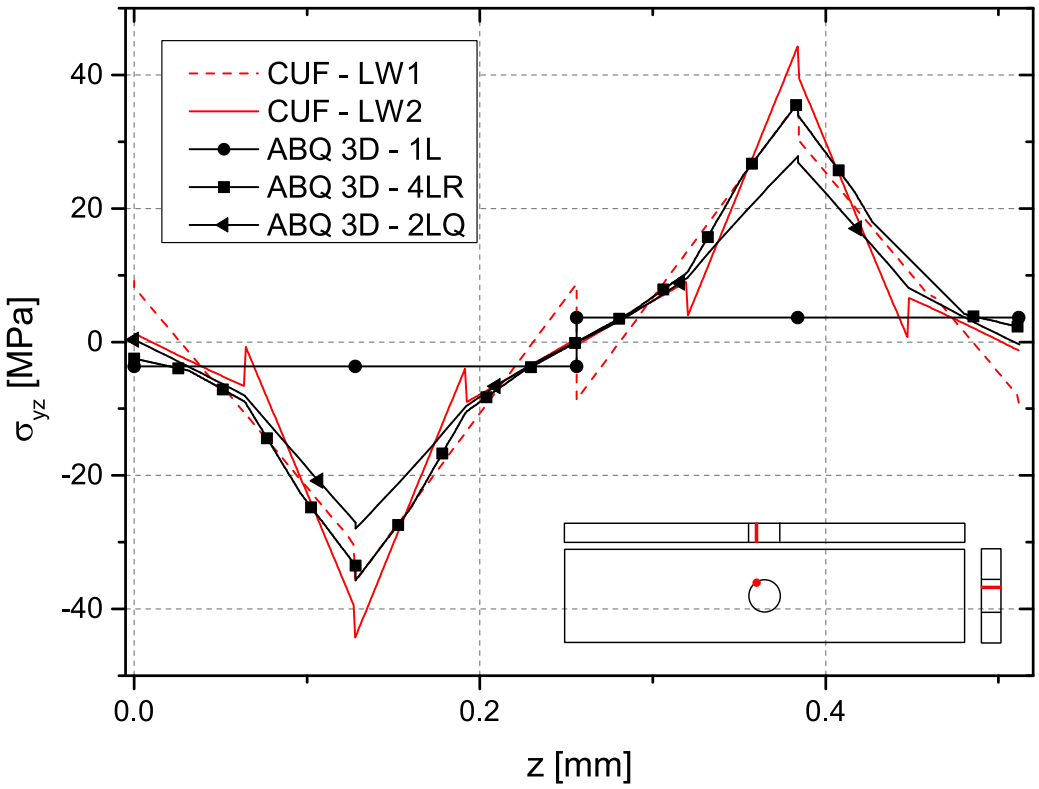

Figure 21: Transverse shear stress distribution σ_{yz} through the thickness of $[0/90]_s$ notched laminate under an applied displacement of 0.125 mm, $x = 17.04$, $y = 68$

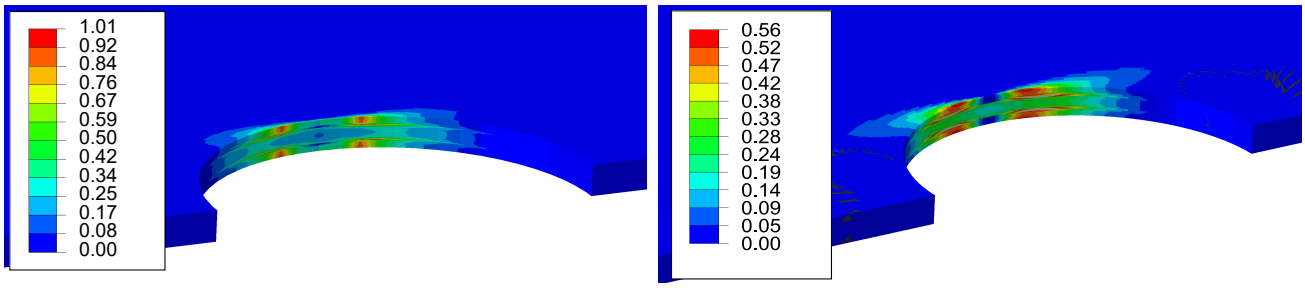

(a) CUF-LW2 (53,346 DOF) **(b)** ABQ3D-4L (1,306,977 DOF)

Figure 22: Hashin3D matrix tension (MT) failure index for $[0/90]_s$ laminate under an applied displacement of 0.125 mm

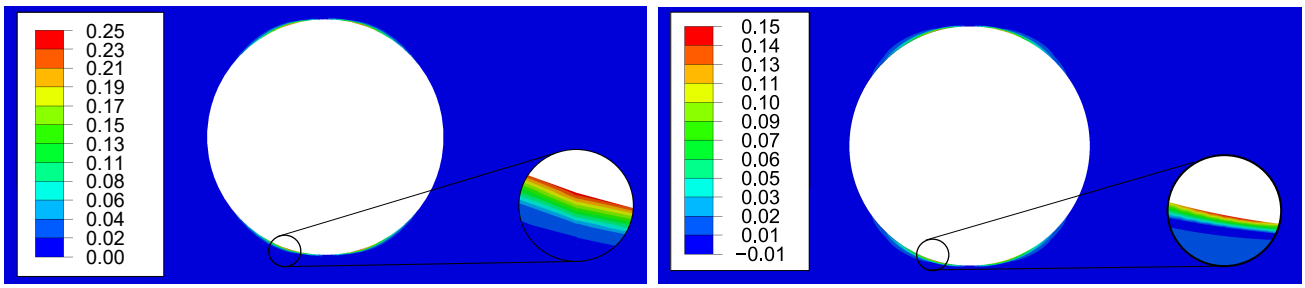

(a) CUF-LW2 (53,346 DOF) **(b)** ABQ3D-4L (1,306,977 DOF)

Figure 23: Delamination failure index for $[0/90]_s$ laminate under an applied displacement of 0.125 mm

σ_{xy} and the out-of-plane shear stresses σ_{yz}, respectively, are underestimated in ABAQUS when compared with the CUF results. This is reflected in the failure index for matrix tension, as shown in Fig. 22, and that of delamination, shown in Fig. 23, where the values reported by ABAQUS are significantly lower than those reported by CUF. As well-known, the use of quadratic brick elements leads to improvement in the stress field with such improvements more evident in the case of the out-of-plane stress components.

4. The refinement of the CUF discretization along the thickness leads to the fulfillment of the top and bottom out-of-plane stress boundary conditions and higher peak values.

4.3 Stringer stiffened panel

The current example evaluates the failure indices for a composite panel stiffened using a composite stringer. The geometry of the structure was taken from [30], and a schematic representation of the cross-section along with the applied boundary conditions is shown in Fig. 24. The length of the specimen is 240 mm. The material system used is IM7/8552, and the properties are listed in Table 1. The skin is composed of an 8-ply quasi-isotropic laminate with a stacking sequence of $[45/90/-45/0]_s$ and a total thickness of 1.0 mm, while the stiffener is composed of a 7-ply laminate whose stacking sequence is given as $[-45/0/45/0/45/0/-45]$ with a thickness of 0.875 mm. The computed failure indices are based on the Hashin 3D failure criteria.

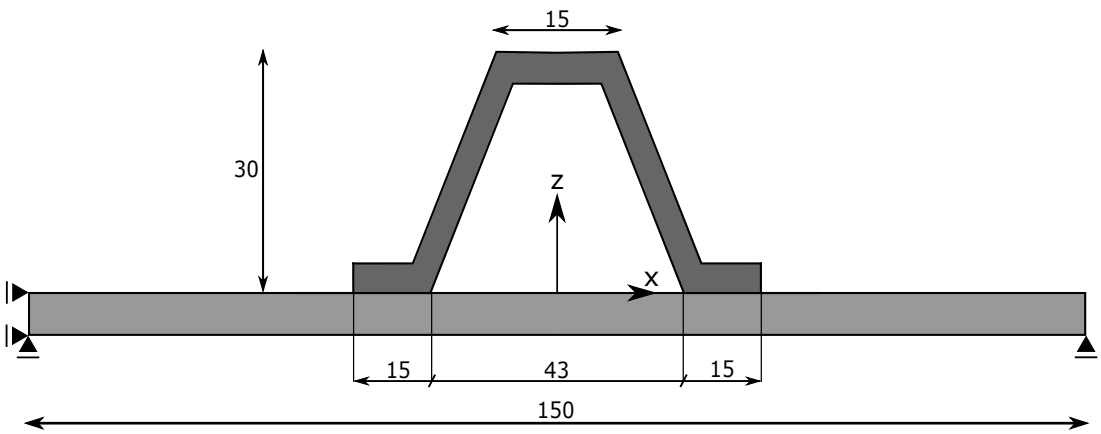

Figure 24: Cross-section of the stringer stiffened panel (dimensions in mm)

A uni-axial tension test was performed on the specimen using CUF-LW, where the model axis was discretized with 10 B4 (cubic) elements. Two cross-section meshes were considered for the analysis: (a) CUF-LW$_1$ - 355 L9 (bi-quadratic) Lagrange elements with one element per ply, and (b) CUF-LW$_2$ - 710 L9 (bi-quadratic) Lagrange elements with two elements per ply, to investigate the effect of cross-section mesh refinement on the analysis. A schematic representation of the cross-section mesh with 1 L9 per ply has been shown in Fig. 25. The stringer was constrained along the y-direction, i.e., $u_y = 0.0$, on one end of the stringer [y = 0.0], and a constraint of $u_x = 0.0$ was applied at the plane [x = -75.0]. Similarly, a constraint of $u_z = 0.0$ was applied on the base i.e. [z = -1.0]. A displacement $u_y = 0.97$ mm was applied on the opposite end [y = 240.0] of the stringer, which corresponds to the load for first ply failure, i.e, one of the failure indices attains the value of unity. The

results obtained from CUF were compared with those of ABAQUS 3D. Two ABAQUS models were considered, where each ply was discretized using one and two linear hexahedral elements, respectively. The results of these analyses were plotted through the thickness, at some salient points of the structure, i.e., point A [x = 36.5, y = 120.0] which is the free-edge of the stringer, and point B [x = 75.0, y = 120.0], which is the free-edge of the skin, see Fig. 26. Model data on the type of mesh, DOF required, and analysis time were listed in Table 8.

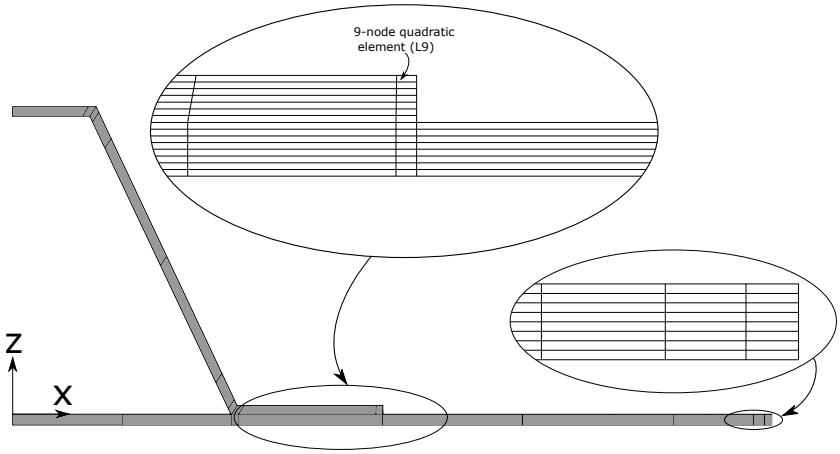

Figure 25: Cross-section mesh used for the CUF-LW$_1$ (one L9 element per ply) analysis. Due to the symmetric nature of the mesh, only the right half has been shown.

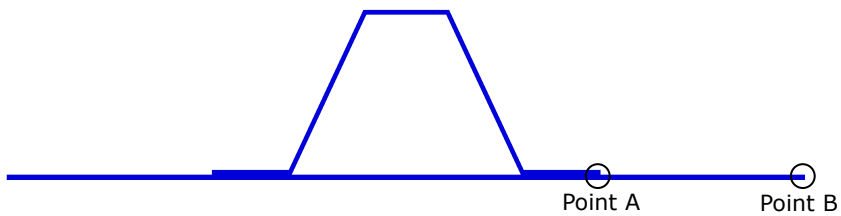

Figure 26: Points of interest in the cross-section of the structure

Table 8: Model information for the stringer analysis

Model	Discretization	DOF	CPU Time [s]
CUF-LW$_1$	355 L9 over the cross-section, with 1 L9 per ply. 10 B4 along y.	142,476	161
CUF-LW$_2$	710 L9 over the cross-section, with 2 L9 per ply. 10 B4 along y.	277,326	478
ABQ-3D$_1$	705,600 linear brick elements (C3D8). One element per ply.	2,422,749	760
ABQ-3D$_2$	1,411,200 linear brick elements (C3D8). Two elements per ply.	4,560,150	3,764

Table 9 shows failure indices for various locations and failure modes. The axial stress σ_{yy} at point A was plotted in Fig. 27, while the out-of-plane stress components in Fig. 28. The Hashin 3D matrix tension failure index and the delamination index were plotted in Fig. 29a and Fig. 29b, respectively. Similarly, the corresponding results were plotted at the free-edge of the skin, i.e., at point B. The axial stress σ_{yy} is shown in Fig. 30, while the out-of-plane stress components are shown in Fig. 31. The failure indices related to matrix tension failure and delamination are shown in Fig. 32. The contour plot of the matrix tension failure index at point B has been shown in Fig. 33, while that of the delamination index is shown in Fig. 34. Similarly,

the contour plots for the matrix tension failure index and delamination index in the region near point A were plotted in Fig. 35 and Fig. 36, respectively.

Table 9: Failure indices via various FE models for the stringer stiffened panel at first ply failure (failure mode: matrix tension)

Mode	Delamination	Matrix Tension	Fibre Tension
Model	Failure index value		
Free edge of stringer [x = 36.5, y = 120.0, z = 0.0125]			
ABQ - $3D_1$	0.1349	0.3817	0.1395
ABQ - $3D_2$	0.2110	0.4358	0.1837
CUF - LW_1	0.5109	0.8681	0.1735
CUF - LW_2	0.5405	0.9307	0.1902
Free edge of skin [x = 75.0, y = 120.0, z = -0.13]			
ABQ - $3D_1$	0.1723	0.6715	0.1808
ABQ - $3D_2$	0.1876	0.6832	0.2074
CUF - LW_1	0.2483	1.0035	0.7143
CUF - LW_2	0.2380	1.0095	0.7574

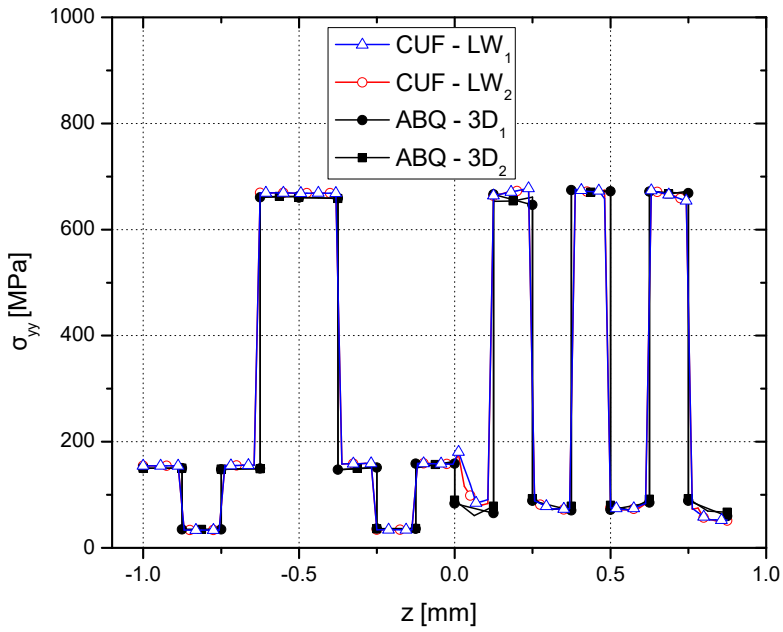

Figure 27: Axial stress σ_{yy} through the thickness at the free-edge (point A)

The following comments can be made based on the results of the above analyses:

1. Free-edge effects are significant, and first ply failure occurs due to matrix failure (in tension) at this region.

2. The discretisation of the plies through the thickness is of importance, significantly influencing the stress fields in the transverse direction. This can be seen in the above results, e.g., in Fig. 31, where increasing the number of elements per ply in the ABAQUS models leads to the results approaching that of CUF modelled using 2 quadratic L9 elements per ply.

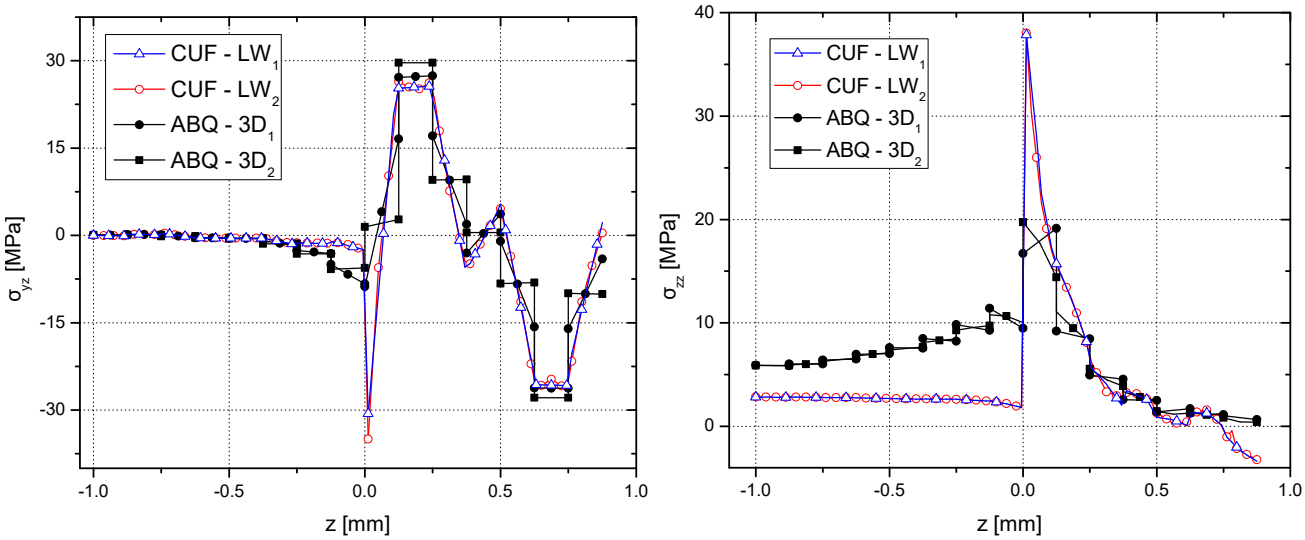

(a) σ_{yz} **(b)** σ_{zz}

Figure 28: Out-of-plane stress components through the thickness at the free-edge (point A)

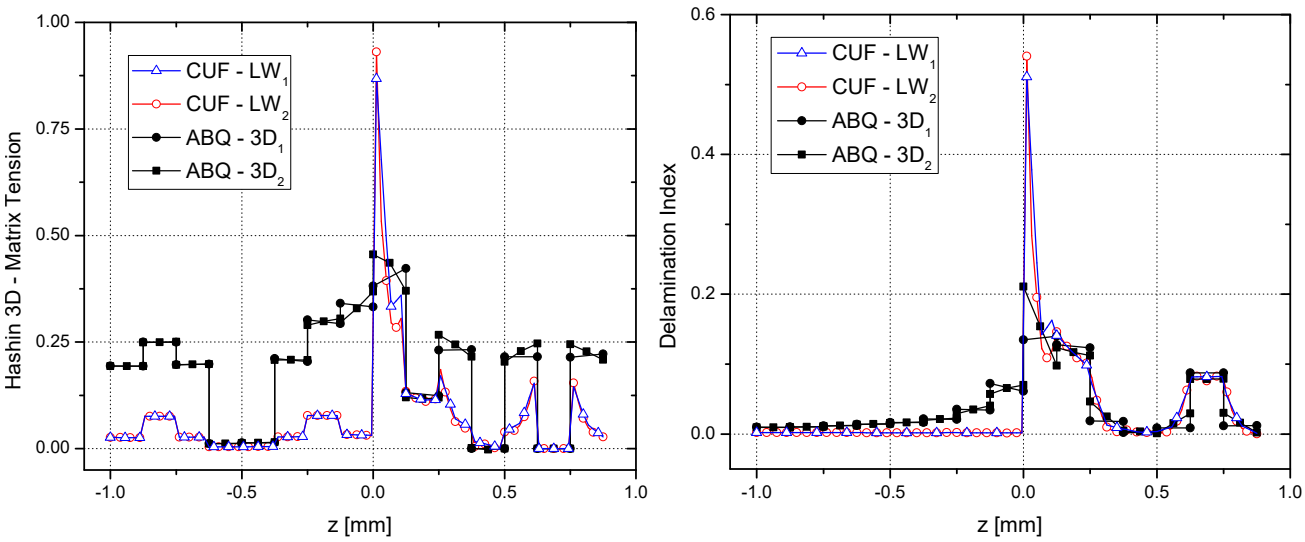

(a) Hashin 3D - Matrix Tension **(b)** Delamination Index

Figure 29: Failure Indices through the thickness at the free-edge (point A)

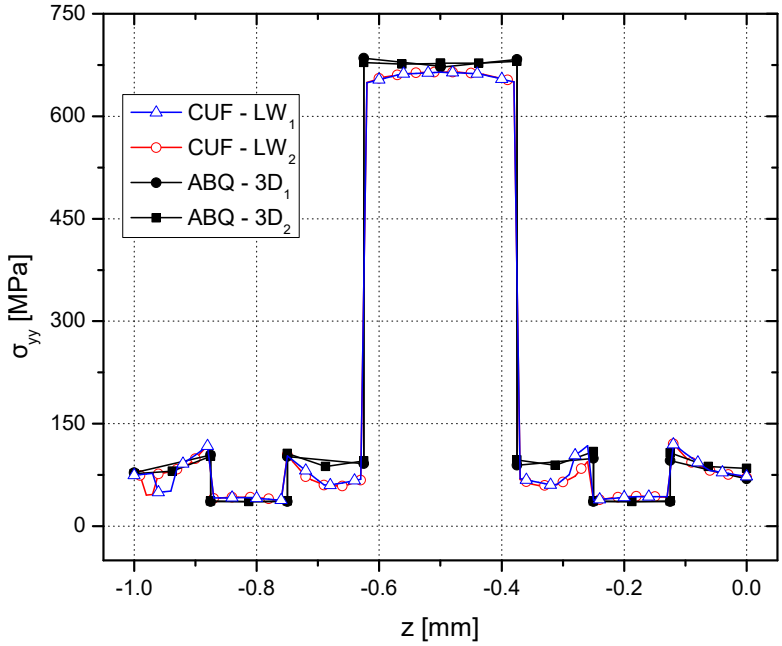

Figure 30: Axial stress σ_{yy} through the thickness at the free-edge of the skin (point B)

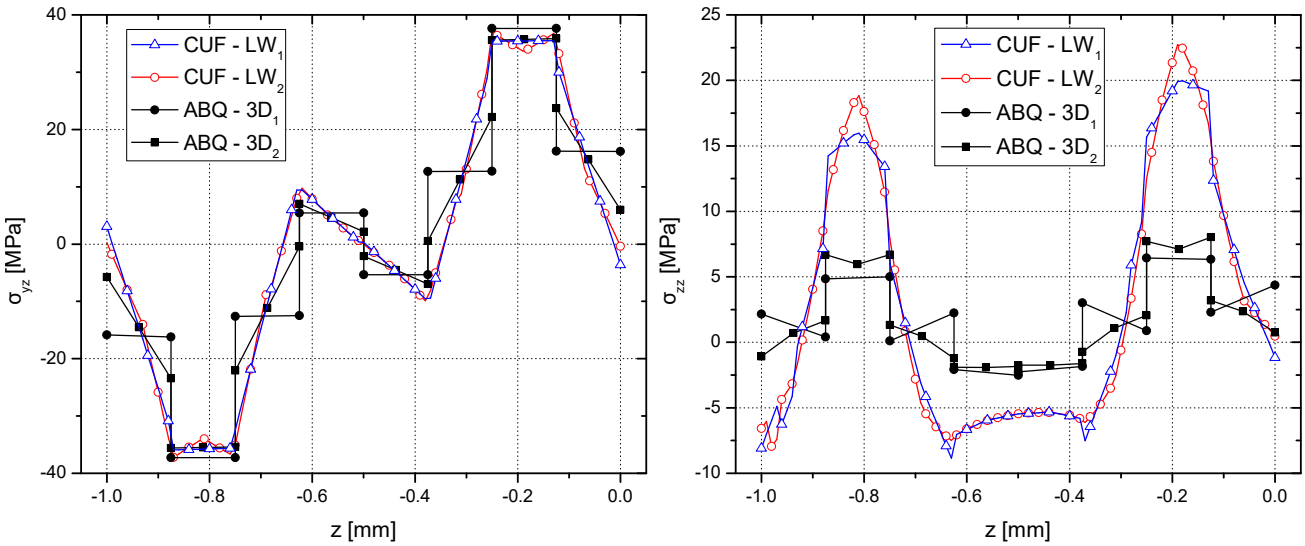

(a) σ_{yz} **(b)** σ_{zz}

Figure 31: Out-of-plane stress components through the thickness at the free-edge of the skin (point B)

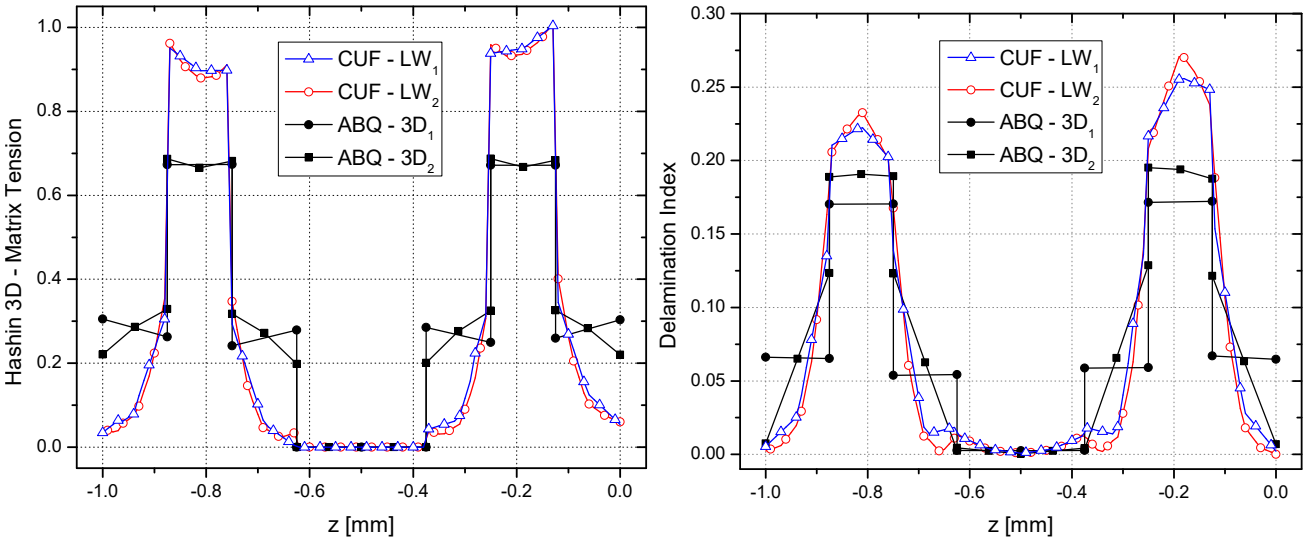

(a) Hashin 3D - Matrix Tension

(b) Delamination Index

Figure 32: Failure Indices through the thickness at the free-edge of the skin (point B)

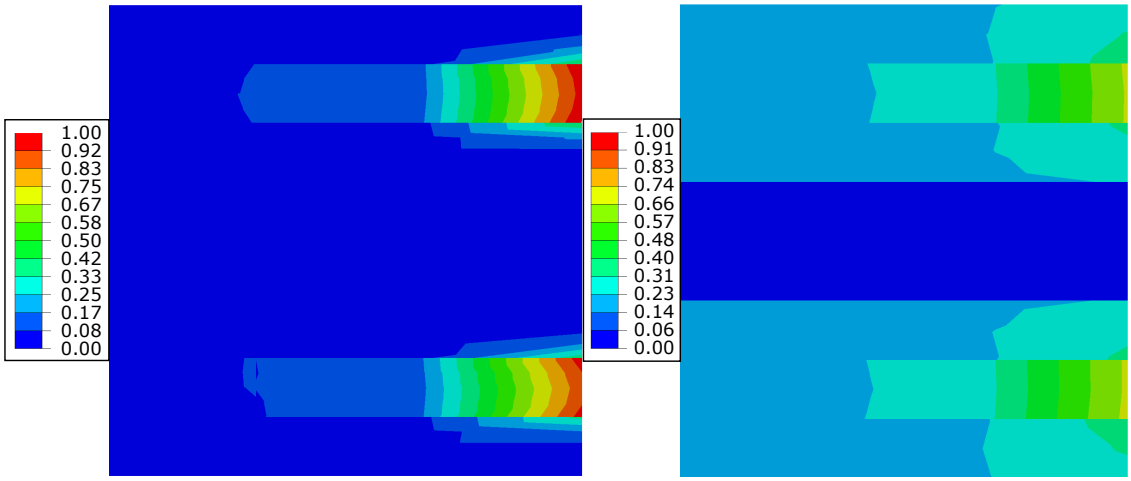

(a) CUF-LW$_2$

(b) ABQ-3D$_2$

Figure 33: Contour plot of Matrix tension failure index through the thickness at the free-edge of the skin (point B)

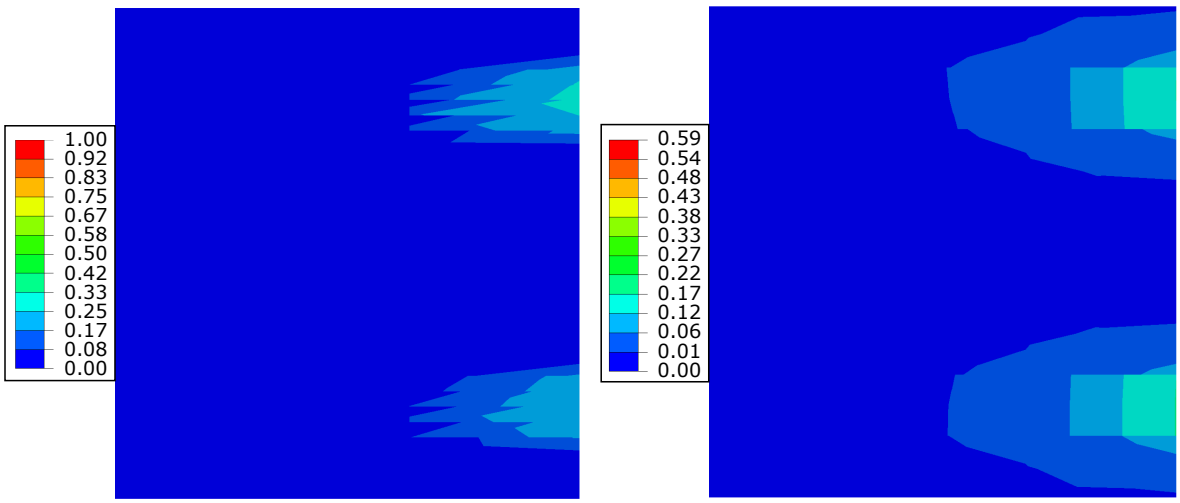

(a) CUF-LW$_2$

(b) ABQ-3D$_2$

Figure 34: Contour plot of the delamination index through the thickness at the free-edge of the skin (point B)

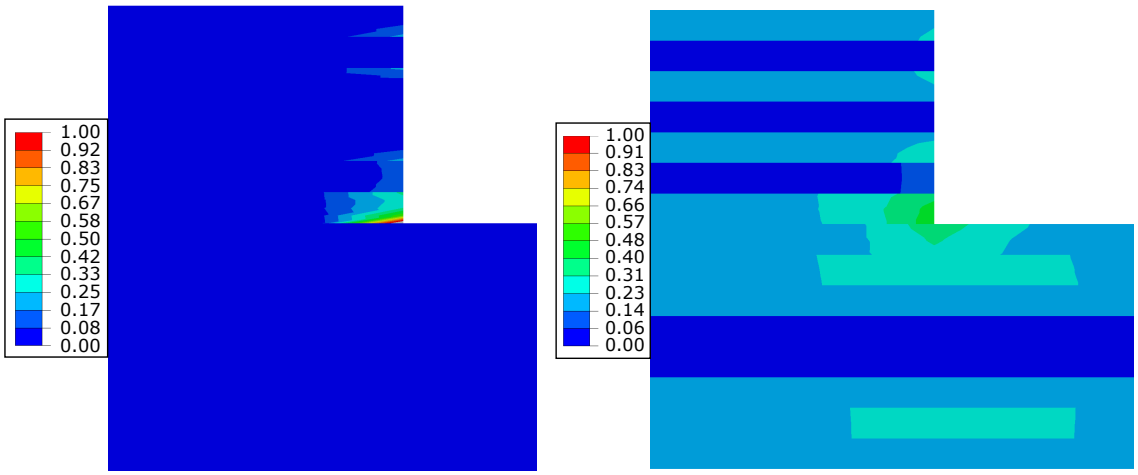

(a) CUF-LW$_2$ **(b)** ABQ-3D$_2$

Figure 35: Contour plot of Matrix tension failure index (point A)

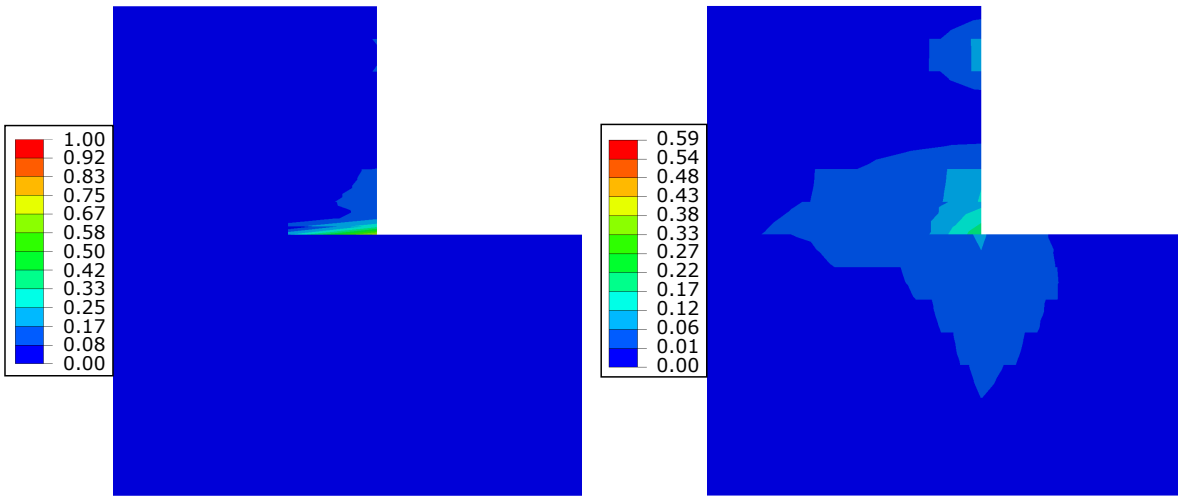

(a) CUF-LW$_2$ **(b)** ABQ-3D$_2$

Figure 36: Contour plot of the delamination index (point A)

3. The cross-section mesh used in the CUF analysis can influence the out-of-plane stress fields as can be seen in Fig. 31b, where the lack of refinement in the CUF-LW$_1$ model results in a smeared or spread-out peak σ_{zz}, as opposed to the CUF-LW$_2$ case. This directly affects indices which are a function of σ_{zz}, such as the delamination index as can be seen in Fig. 32b, where the CUF-LW$_1$ model predicts a spread-out peak index which is smaller in magnitude when compared to the CUF-LW$_2$ case.

4. A full 3D FEA using traditional FE can lead to prohibitively high computational costs, whereas CUF leads to more accurate results in a more computationally efficient manner. The use of higher-order theories to expand the cross-section kinematics is of great importance to enhancing efficiency.

5. A peak of σ_{zz} was found at the corner between the stringer and the skin. In particular, such a peak appears at the intersection between the interior of the skin, where no peaks are observed, and the free-edge of the stiffener, where the stress concentrations arise due to the sudden change of the stress fields in the bonded area.

5 Conclusions

A failure evaluation of composite laminated structures has been performed via 1D and 3D FE and failure indices computed using the Hashin 3D failure criterion. 1D elements have been built via CUF, where the beam cross-section kinematics is enhanced using Lagrange polynomials, resulting in an LW modeling of the composite laminates. 3D FE models have been built in ABAQUS. The failure indices have been used as a parameter to determine the onset of failure via first ply failure. In particular, the onset of delamination has been predicted using a delamination index computed using the quadratic mixed mode criterion. The following observations can be made based on the results of the numerical analysis:

1. An accurate evaluation of the 3D stress field, especially the out-of-plane terms around free-edges, is of great importance to computing failure indices.

2. In a 3D FE model, the requirement for the accurate evaluation of the out-of-plane stress may lead to prohibitive computational costs, especially for large composite structures with fairly complicated geometry.

3. The use of higher-order 1D models in CUF results in a 3D-like accuracy of the stress solutions, at a significantly reduced computation cost if compared to 3D elements. CUF requires some 10 to 20 times less DOF than 3D elements.

4. The CUF capability of improving the modeling accuracy via refinement of the displacement field along the thickness is decisive as far as the out-of-plane stress distributions are considered.

Future works should include physically non-linear analyses and the extension to global-local approaches.

Acknowledgments

This research work has been carried out within the project FULLCOMP (Fully Integrated Analysis, Design, Manufacturing, and Health-Monitoring of Composite Structures), funded by the European Union Horizon 2020 Research and Innovation program under the Marie Skłłodowska-Curie Grant agreement No. 642121, and project ICONIC (Improving the Crashworthiness of Composite Transportation Structures), funded by the European Union Horizon 2020 Research and Innovation program under the Marie Skłłodowska-Curie Grant agreement No. 721256.

References

[1] S.W. Tsai and H.T. Hahn. Failure analysis of composite materials. In *Winter annual meeting of ASME*, pages 73–96, 1975.

[2] J.N. Reddy and A.K. Pandey. A first-ply failure analysis of composite laminates. *Computers & Structures*, 25(3):371–393, 1987.

[3] Y.S.N. Reddy and J.N. Reddy. Linear and non-linear failure analysis of composite laminates with transverse shear. *Composites Science and Technology*, 44(3):227–255, 1992.

[4] J.H. Park, J.H. Hwang, C.S. Lee, and W. Hwang. Stacking sequence design of composite laminates for maximum strength using genetic algorithms. *Composite Structures*, 52(2):217–231, 2001.

[5] J. Huang and R.T. Haftka. Optimization of fiber orientations near a hole for increased load-carrying capacity of composite laminates. *Structural and Multidisciplinary Optimization*, 30(5):335–341, 2005.

[6] S.K. Panigrahi and B. Pradhan. Three dimensional failure analysis and damage propagation behavior of adhesively bonded single lap joints in laminated FRP composites. *Journal of Reinforced plastics and Composites*, 26(2):183–201, 2007.

[7] B.G. Kiral. Effect of the clearance and interference-fit on failure of the pin-loaded composites. *Materials & Design*, 31(1):85–93, 2010.

[8] V. Tita, J. De Carvalho, and D. Vandepitte. Failure analysis of low velocity impact on thin composite laminates: Experimental and numerical approaches. *Composite Structures*, 83(4):413–428, 2008.

[9] A. Levi-Sasson, J. Aboudi, A. Matzenmiller, and R. Haj-Ali. Failure envelopes for laminated composites by the parametric HFGMC micromechanical framework. *Composite Structures*, 140:378–389, 2016.

[10] Y.S. Reddy and J.N. Reddy. Three-dimensional finite element progressive failure analysis of composite laminates under axial extension. *Journal of Composites, Technology and Research*, 15(2):73–87, 1993.

[11] N. Silvestre and D. Camotim. First-order generalised beam theory for arbitrary orthotropic materials. *Thin-Walled Structures*, 40(9):755–789, 2002.

[12] N. Silvestre and D. Camotim. Second-order generalised beam theory for arbitrary orthotropic materials. *Thin-Walled Structures*, 40(9):791–820, 2002.

[13] W. Yu, V.V. Volovoi, D.H. Hodges, and X. Hong. Validation of the variational asymptotic beam sectional analysis. *AIAA journal*, 40(10):2105–2112, 2002.

[14] R. El Fatmi. On the structural behavior and the saint venant solution in the exact beam theory. application to laminated composite beams. *Computers & Structures*, 80(16-17):1441–1456, 2002. doi: 10.1016/S0045-7949(02)00090-1.

[15] P. Ladéveze, P. Sanchez, and J. Simmonds. Beamlike (Saint-Venant) solutions for fully anisotropic elastic tubes of arbitrary closed cross section. *Internatinal Journal of Solids & Structures*, 41(7):1925–1944, 2004. doi: 10.1016/j.ijsolstr.2003.11.006.

[16] S.B. Dong, C. Alpdogan, and E. Taciroglu. Much ado about shear correction factors in timoshenko beam theory. *International Journal of Solids and Structures*, 47(13):1651 – 1665, 2010.

[17] E. Carrera, M. Cinefra, M. Petrolo, and E. Zappino. *Finite element analysis of structures through unified formulation.* John Wiley & Sons, 2014.

[18] P. Nali and E. Carrera. A numerical assessment on two-dimensional failure criteria for composite layered structures. *Composites Part B: Engineering*, 43(2):280–289, 2012.

[19] M. Maiarú, M. Petrolo, and E. Carrera. Evaluation of energy and failure parameters in composite structures via a component-wise approach. *Composites Part B: Engineering*, 108:53–64, 2017.

[20] E. Carrera and M. Petrolo. Refined one-dimensional formulations for laminated structure analysis. *AIAA Journal*, 50(1):176–189, 2012.

[21] E. Zappino and E. Carrera. Multidimensional model for the stress analysis of reinforced shell structures. *AIAA Journal*, 56(4):1647–1661, 2018.

[22] J.N. Reddy. *Mechanics of laminated composite plates and shells. Theory and Analysis.* CRC Press, 2nd edition, 2004.

[23] Z. Hashin. Failure criteria for unidirectional fiber composites. *Journal of applied mechanics*, 47(2):329–334, 1980.

[24] J.C. Brewer and P.A. Lagace. Quadratic stress criterion for initiation of delamination. *Journal of composite materials*, 22(12):1141–1155, 1988.

[25] ASTM International, West Conshohocken, PA. *ASTM D3039/D3039M-17 Standard Test Method for Tensile Properties of Polymer Matrix Composite Materials*, 2017.

[26] A.S.D. Wang and Frank W. Crossman. Some new results on edge effect in symmetric composite laminates. *Journal of Composite Materials*, 11(1):92–106, 1977.

[27] M. Cho and H.S. Kim. Iterative free-edge stress analysis of composite laminates under extension, bending, twisting and thermal loadings. *International Journal of Solids and Structures*, 37(3):435 – 459, 2000.

[28] L. Lagunegrand, T. Lorriot, R. Harry, H. Wargnier, and J.M. Quenisset. Initiation of free-edge delamination in composite laminates. *Composites Science and Technology*, 66(10):1315 – 1327, 2006.

[29] E. Martin, D. Leguillon, and N. Carrere. A twofold strength and toughness criterion for the onset of free-edge shear delamination in angle-ply laminates. *International Journal of Solids and Structures*, 47(9):1297 – 1305, 2010.

[30] C. Bisagni, R. Vescovini, and C. G. Dávila. Single-stringer compression specimen for the assessment of damage tolerance of postbuckled structures. *Journal of Aircraft*, 48(2):495–502, 2011.